

# A shallow cross-flow fluidized-bed solar reactor for continuous calcination processes



Thibaut Esence, Hadrien Benoit, Damien Poncin, Michael Tessonnaud, Gilles Flamant\*

Processes, Materials and Solar Energy Laboratory, (PROMES-CNRS, UPR 8521), 7 Rue du Four Solaire, Odeillo, 66120 Font-Romeu, France

## ARTICLE INFO

### Keywords:

Solar heat in industrial process  
Calcination  
Cross-flow fluidized bed  
Experiment  
Modelling

## ABSTRACT

A laboratory-scale solar reactor prototype dedicated to calcination processes of non-metallic mineral particles is tested and characterized. The prototype consists of an indirect heating shallow cross-flow fluidized-bed reactor-receiver. It is composed of 4 compartments in series in which the particles are thermally treated with solar power in order to drive the endothermic calcination reaction. The particles are fluidized in the reactor with preheated air and are heated up to 800 °C through the front wall of the reactor receiving the concentrated solar flux (about 200 kW/m<sup>2</sup>). The tests are carried out at the 1-MW Odeillo's solar furnace (France). The thermal decomposition of a continuous stream of 9.4 kg/h of dolomite (CaMg(CO<sub>3</sub>)<sub>2</sub>) is investigated in this paper. The half decomposition of dolomite (CaMg(CO<sub>3</sub>)<sub>2</sub> → CaCO<sub>3</sub> + MgO + CO<sub>2</sub>) is performed with a degree of conversion of 100%. The complete decomposition of dolomite (CaMg(CO<sub>3</sub>)<sub>2</sub> → CaO + MgO + 2CO<sub>2</sub>) is not reached because, with respect to the CO<sub>2</sub> partial pressure in the reactor, the temperature of particles is not high enough to decompose the calcium carbonate. The calculated thermochemical efficiency (i.e. the energy absorbed by the endothermic calcination reaction compared to the solar energy provided to the system) is 6.6%. This low efficiency is neither surprising nor critical since the reactor design was not optimised with respect to energy efficiency but designed to the control of particle flow and front wall solar flux distribution. A numerical model considering the 4 compartments of the reactor as 4 ideal continuous stirred tank reactors in series is developed. The model accounts for the mass and the energy balances, as well as the reaction kinetics of the half decomposition of dolomite. The model gives consistent results compared to the experimental data. These results are a proof of concept of continuous calcination reaction using concentrated solar energy in a cross-flow fluidized-bed reactor.

## 1. Introduction

Thermal decomposition of minerals at high temperature is used in various industrial sectors (lime, cement clinker, phosphates, metallurgy, glass industry, etc.). The minerals are usually crushed and treated in rotary kilns or fluidized bed reactors. Nowadays, the heat required to drive the process is mainly provided by the combustion of gas, coal or alternative carbonaceous fuels. Consequently, this industrial sector is the second larger contributor of anthropogenic greenhouse gases after power generation by combustion. Therefore, using renewable heat sources in such processes would considerably reduce the environmental impact of many industrial sectors.

Concentrated Solar Power is increasingly used for power generation. This technology is also promising as a high temperature renewable heat source to replace fossil fuels in industrial applications. Among these applications, calcination for lime, dolomite and cement processing is a critical target for solar heat because it is responsible of about 8% of

worldwide anthropogenic CO<sub>2</sub> emission (Olivier et al., 2016). In traditional processes, the heat of reaction at about 850–900 °C is supplied by combustion of carbon-based fuels. Under these conditions, 40% of the CO<sub>2</sub> emissions of the cement industry are due to the combustion, while it is 20–40% in the lime industry depending on the kiln used (Kumar et al., 2007; Mahasenan et al., 2003). Consequently, solar calcination can save up to 40% of the CO<sub>2</sub> emissions of this industrial sector.

In industry, two main types of kilns are generally used for lime production, shaft kilns and rotary kilns, but shaft kilns dominate the market (Oates, 1998; Stork et al., 2014). Transport reactors such as circulating fluidized bed and cyclones are also used (Havryliv and Maystruk, 2017). For solar applications, three types of solar calcination reactors have been designed and tested, namely the rotary kiln, the cyclone and the fluidized bed. They differ with respect to processed particle size, operation mode (batch or continuous) and solar heating type (direct or indirect). Moumin et al., 2019, analysed the literature

\* Corresponding author.

E-mail address: [gilles.flamant@promes.cnrs.fr](mailto:gilles.flamant@promes.cnrs.fr) (G. Flamant).

<https://doi.org/10.1016/j.solener.2019.12.029>

Received 23 August 2019; Received in revised form 5 December 2019; Accepted 8 December 2019

Available online 21 December 2019

0038-092X/ © 2019 The Authors. Published by Elsevier Ltd on behalf of International Solar Energy Society. This is an open access article under the CC BY license (<http://creativecommons.org/licenses/by/4.0/>).

Nomenclature			
<i>Latin characters</i>			
A	pre-exponential factor [ $s^{-1}$ ]	$\varepsilon_{sol}$	absorptivity of the reactor wall in the solar wavelengths [-]
C	concentration factor [-]	$\eta$	efficiency [-]
DNI	Direct Normal Irradiation [ $W \cdot m^{-2}$ ]	$\lambda$	thermal conductivity [ $W \cdot m^{-1} \cdot K^{-1}$ ]
$d_{3,2}$	Sauter mean diameter (diameter of the sphere with the same volume/surface area ratio) [m]	$\rho$	density [ $kg \cdot m^{-3}$ ]
$d_x$	particle diameter at x% in the cumulative distribution [m]	$\sigma$	Stephan-Boltzmann constant, $\sigma = 5.67 \cdot 10^{-8} W \cdot m^{-2} \cdot K^{-4}$
E	residence time distribution of the particles in a compartment [-]	$\tau_p$	mean residence time of the particles in a reactor compartment [s]
$E_a$	activation energy [ $J \cdot mol^{-1}$ ]	$\Phi$	thermal power [W]
e	thickness [m]	$\varphi$	heat flux [ $W \cdot m^{-2}$ ]
G	Gibbs free enthalpy [ $J \cdot mol^{-1}$ ]	<i>Subscripts</i>	
H	specific enthalpy [ $J \cdot kg^{-1}$ ]	abs	absorbed by the reactor wall
h	convective heat transfer coefficient [ $W \cdot m^{-2} \cdot K^{-1}$ ]	air	related to air
k	reaction rate constant [ $s^{-1}$ ]	amb	related to ambient
M	molar mass [ $kg \cdot mol^{-1}$ ]	B	related to the back wall of the reactor
m	mass [kg]	CaCO <sub>3</sub>	related to calcite
$\dot{m}$	mass flow rate [ $kg \cdot s^{-1}$ ]	CaMg(CO <sub>3</sub> ) <sub>2</sub>	related to dolomite
$\dot{n}$	molar flow rate [ $mol \cdot s^{-1}$ ]	CO <sub>2</sub>	related to carbon dioxide
P	pressure [Pa]	conv	related to the convection
R	universal gas constant, $R = 8.314 J \cdot mol^{-1} \cdot K^{-1}$	eq	related to the equilibrium state
$R_B$	heat transfer resistance of the backward of the reactor [ $m^2 \cdot K \cdot W^{-1}$ ]	ext	related to the external walls of the reactor
S	surface area [ $m^2$ ]	F	related to the front wall of the reactor
T	temperature [K]	FB	related to the fluidized bed
t	time [s]	IR	related to infrared radiations
$t^*$	threshold time [s], see Eq. (14)	i	related to the component <i>i</i>
V	volume of a compartment [ $m^3$ ]	in	related to the inlet
y	mass fraction [-]	ins	related to the insulation
<i>Greek characters</i>		max	maximum value
$\alpha$	degree of conversion [-]	MgO	related to magnesium oxide
$\bar{\alpha}$	average degree of conversion of a compartment [-]	n	related to the compartment number <i>n</i>
$\gamma$	volume fraction of particles in a reactor compartment [-]	out	related to the outlet
$\Delta H_r$	reaction enthalpy [ $J \cdot mol^{-1}$ ]	p	related to the particles
$\varepsilon_{IR}$	emissivity of the reactor wall in the infrared wavelengths	r	related to the reaction
		sol	related to the solar wavelengths
		th	thermal
		thch	thermochemical
		tot	total value

data according to particle size. Cyclone reactors have been used to process continuously small particles, with diameter typically less than 10  $\mu m$  (Imhof, 2000, 1997; Nikulshina et al., 2009; Steinfield et al., 1991). Rotary kilns enable to calcine particles with a wide range of diameters, generally from 100  $\mu m$  to some mm (Abanades and André, 2018; Flamant et al., 1980; Meier et al., 2006). Moumin et al., 2019, have successfully calcined small cement raw meal particles in a rotary solar reactor. Finally, fluidized beds can process about 100–500  $\mu m$  particles with a narrow size distribution (Flamant et al., 1980; Tregambi et al., 2018). According to Table 1, only batch operations have been tested with solar fluidized beds. Moreover, only experimental data from vertical column containing fluidized beds directly heated by concentrated solar energy have been reported. With respect to this state-of-the-art on solar calcination reactors, this study proposes four main innovations: compartmented fluidized bed, continuous

operation, indirect heating of the particles, solar power larger than 10 kW. Particle residence time distribution (RTD) in cross-flow fluidized beds (with one, two and four compartments) was examined by Kong et al. (2018). They showed that a cascade of perfectly mixed reactors or a plug flow with dispersion model can be applied to describe the RTD.

This paper investigates a new concept of solar reactor-receiver for the processing of reactive particulates. A shallow cross-flow compartmented fluidized-bed reactor has been designed and tested at the 1-MW Odeillo's solar furnace in France. The aim of these tests is to show the feasibility of continuous calcination processes with concentrated solar energy. In particular, the thermal decomposition of dolomite (CaMg(CO<sub>3</sub>)<sub>2</sub>) is investigated.

The experimental data are used to validate a numerical model aiming at studying the design parameters of the system. This model

**Table 1**  
Tested fluidized bed calcination solar reactors.

Author	Particle	Operation	Solar irradiation	Typical power
Flamant et al., 1980	Calcite	Batch	Direct	1.7 kW
Tregambi et al., 2018	Calcite	Batch	Direct	3.2 kW
This study	Dolomite	Continuous	Indirect	25 kW

accounts for the mass and the energy balances of the reactor-receiver during reactive particles processing. For that purpose, it is necessary to model the reaction kinetics of dolomite decomposition. The thermal decomposition of dolomite into magnesium oxide and lime ( $\text{CaMg}(\text{CO}_3)_2 \rightarrow \text{MgO} + \text{CaO} + 2 \text{CO}_2$ ) has been investigated by many authors (Haul and Heystek, 1952; Olszak-Humienik and Jablonski, 2015; Subagio et al., 2017; Valverde et al., 2015). Several studies showed that the decomposition of dolomite under air is a one-step process occurring at about 750 °C (Fazeli and Tareen, 1991; Gunasekaran and Anbalagan, 2007; Samtani et al., 2001; Valverde et al., 2015). However, if the reaction occurs under atmospheres with a significant partial pressure of carbon dioxide, the reaction becomes a two-step process. First, the dolomite is decomposed into magnesium oxide and calcite ( $\text{CaMg}(\text{CO}_3)_2 \rightarrow \text{MgO} + \text{CaCO}_3 + \text{CO}_2$ ). This step is almost not affected by the  $\text{CO}_2$  partial pressure. Then, calcite is decomposed into lime ( $\text{CaCO}_3 \rightarrow \text{CaO} + \text{CO}_2$ ) at higher temperature depending on the  $\text{CO}_2$  partial pressure. Because of crystalline structure differences, the decomposition of  $\text{CaCO}_3$  derived from the half-decomposition of dolomite occurs 10–15 °C lower than the thermal decomposition of  $\text{CaCO}_3$  from limestone (Valverde et al., 2015). The two-step decomposition of dolomite occurs when the  $\text{CO}_2$  partial pressure exceeds 0.13 atm (Haul and Heystek, 1952), which is approximately the equilibrium  $\text{CO}_2$  partial pressure of the calcination/carbonation of calcite at 750 °C. Because of interactions between both compounds and structure differences, the reaction kinetics of dolomite decomposition is different from pure magnesite and pure calcite decompositions (Dennis and Hayhurst, 1987; Haul and Markus, 1952; Mårtensson and Bjerle, 1996; Valverde et al., 2015). Moreover, it is significantly affected by the particle size: the smaller the particles, the higher is the conversion rate (Demir et al., 2003; Hehl et al., 1983; Mårtensson and Bjerle, 1996; Samtani et al., 2001; Steen et al., 1980). Several authors investigated the mechanisms governing this reaction (Dennis and Hayhurst, 1987; Hashimoto et al., 1980; McIntosh et al., 1990; Rodriguez-Navarro et al., 2012). Hehl et al., 1983, tested the dolomite decomposition in a fluidized-bed reactor and showed that it is possible to separate and to control the two steps of the calcination reaction by adapting the operating conditions, especially the residence time of the particles and the fluidization air flow rate (which affects the  $\text{CO}_2$  partial pressure in the reactor). Some authors proposed a reaction kinetics specifically dedicated to the first decomposition of dolomite (into magnesium oxide and calcite) but showed that it depends a lot on the experimental operating conditions (size of the particles, size of the sample, heating rate). These results are

therefore difficult to use and to extrapolate to other experimental conditions. Consequently, the reaction kinetics of the first decomposition of dolomite can only be estimated for purpose of modelling.

The paper presents first the experimental setup, the operating procedure and the particle characteristics. The numerical model accounting for the reaction kinetics and the residence time distribution of the particles inside the reactor is then introduced. Representative experimental results are detailed and compared to the simulated data in the last paragraph. Efficiencies of the reactor prototype are also evaluated.

## 2. Experimental setup

### 2.1. Reactor-receiver

The experimental setup consists of a shallow cross-flow reactor-receiver composed of four compartments in series in which the solid particles are fluidized with air (Fig. 1). The reactor is compartmented in order to reduce the dispersion of the particle residence time distribution and thus to increase the homogeneity of the product conversion. The particles are fed with a vibrator into the reactor, they successively pass through the 4 compartments and overflow to the outlet. The fluidization air is injected at the bottom of the reactor through two perforated tubes. The air and the carbon dioxide produced by the reaction are then sucked at the top of the reactor toward a bag filter.

The reactor is made of stainless steel AISI 310S. It is 1000 mm long (4 compartments, 250 mm long), 80 mm wide and 165 mm high. The outlet tube and the separations of the compartments are designed to limit the fluidized bed height at about 100 mm, above this height, the particles overflow to the next compartment or to the outlet of the reactor. The fluidized bed volume in the reactor is therefore about 8 l, which corresponds approximately to 9 kg of particles assuming a solid volume fraction of 40%.

Each distribution tube of 10 mm diameter is perforated with two staggered sideways rows of 24 holes (96 holes in total). The holes have a diameter of 0.7 mm, are regularly spaced over the tube length and are slightly oriented towards the bottom of the reactor with a 30° angle from the horizontal.

The front wall of the reactor is heated up by the concentrated solar power. The heat absorbed by the wall is transferred by conduction, convection and radiation to the fluidized bed and provides the sensible heat and the reaction enthalpy driving the endothermic calcination

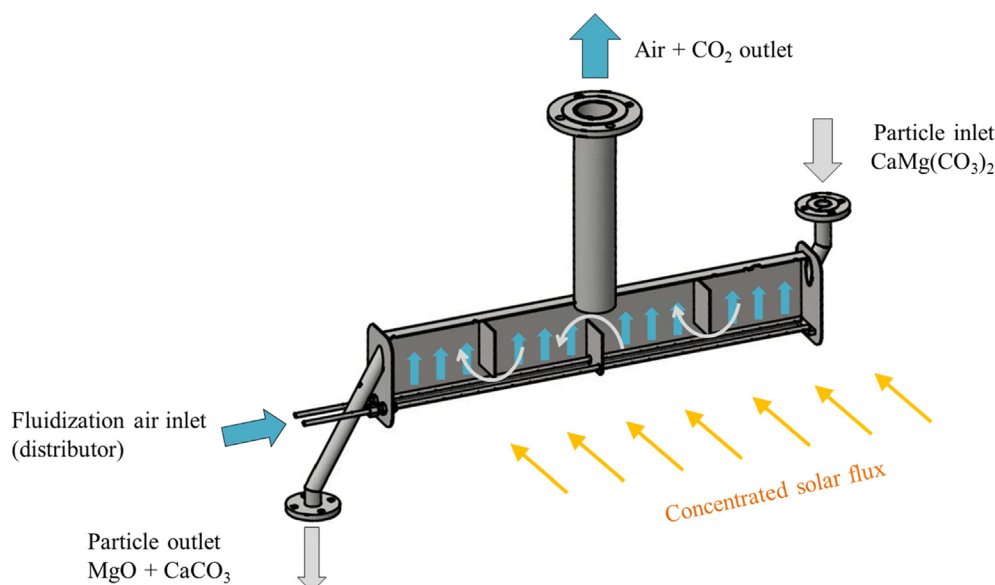


Fig. 1. Cut view of the reactor-receiver with principle of particle and gas flows.

reaction. The back wall of the reactor is thermally insulated with 100 mm of mineral wool with an average thermal conductivity of  $0.2 \text{ Wm}^{-1}\text{K}^{-1}$ .

Preliminary tests showed that fluidization air taken at ambient temperature hinders the reactor from reaching temperatures high enough for the calcination reaction. Consequently, the fluidization air is preheated by passing through pipes inside the insulation of the back wall of the reactor.

## 2.2. Instrumentation

The reactor is equipped with 32 K-type thermocouples: 14 thermocouples are welded on the front wall, 4 thermocouples are welded on the back wall, and 14 thermocouples are distributed inside the reactor to monitor the temperature of the fluidized particles. Pressure sensors are used to measure the pressure drop of the bed and a flowmeter measures the mass flow rate of fluidization air.

## 2.3. Solar facility

The setup was implemented and tested at the focus of the 1-MW Odeillo's solar furnace (France) (Fig. 2).

For the purpose of the test campaign, the heliostat configuration was calibrated to provide a homogeneous concentrated solar flux to the reactor front wall. The homogeneity of the flux is a key point in such experiments since it enables to rise the average temperature of the reactor front wall while avoiding hot spots that could damage the setup due to overheating.

The calibration was carried out by using a flux bar and a CCD camera. The flux bar consists in a rectangular panel coated with a diffusive painting. The centre of the bar is equipped with a fluxmeter that was used to correlate the flux received by the bar to the grey level recorded by the camera. Then, a heliostat configuration enabling to reach a homogeneous  $\times 200$  concentration ( $\pm 5\%$  depending on the reactor compartment) on the reactor wall has been calibrated. The flux distribution measured with the selected heliostat configuration is depicted in Fig. 3. This shows that the flux is relatively uniform. Some minor heterogeneities are visible, especially a cold spot (around  $150 \text{ kW/m}^2$ ) at the end of compartment 4. From compartment 1 to 4, the average concentration factors are respectively 195, 210, 190 and 195.

## 2.4. Operating conditions

During a test, the steady state conditions are evaluated when the Direct Normal Irradiation (DNI), the temperatures (of the wall and of the particles), the inlet and outlet particle flow rates, and the air flow

rate are constant during more than 30 min. The experimental data presented in this paper were obtained after such a period, 200 min after the beginning of the exposure of the reactor to the concentrated solar flux.

Steady-state conditions with a DNI around  $945 \text{ W/m}^2$  and a fluidized-bed temperature up to  $800 \text{ }^\circ\text{C}$  were reached. During this period, the reactor was fed with a flow rate of dolomite of  $9.4 \text{ kg/h}$ . Over the whole test,  $30.1 \text{ kg}$  of particles were recovered at the reactor outlet. In the meanwhile,  $13.3 \text{ kg}$  of entrained fine particles were recovered in the bag filter connected to the gas extraction.

XRD analyses of outlet samples shows that there were neither  $\text{MgCO}_3$  nor  $\text{CaO}$  at the reactor outlet. This means that the  $\text{MgCO}_3$  contained in dolomite was totally converted into  $\text{MgO}$ , while the  $\text{CaCO}_3$  remained intact. This is because the carbon dioxide produced by the reaction exclusively hinders the calcium carbonate decomposition into lime. As a consequence, the fluidized-bed temperature reached during the test was not high enough to perform the calcium carbonate decomposition and only the half decomposition of dolomite was carried out.

The fluidization air flow rate was set to  $4 \text{ Nm}^3/\text{h}$  at the beginning of the heating process and was progressively decreased as the reaction rate, and hence the  $\text{CO}_2$  production, increased. During the steady-state period, the air flow rate preheated at  $630 \text{ }^\circ\text{C}$  was kept constant at  $1.3 \text{ Nm}^3/\text{h}$ . Considering the average temperature of  $630 \text{ }^\circ\text{C}$  and the ambient pressure of  $850 \text{ hPa}$ , this lead to a superficial fluidization velocity around  $1.8 \text{ cm/s}$ . Depending on the correlations from the literature (Geldart, 1986; Thonglimp et al., 1984; Wen and Yu, 1966), this is between 2.4 and 4.3 times the minimum fluidization velocity. Considering the additional  $\text{CO}_2$  stream produced by the reaction ( $1.1 \text{ Nm}^3/\text{h}$  assuming the complete decomposition of magnesium carbonate), this was enough to get a good fluidization regime.

## 3. Material characterization

The presented test was carried out with dolomite from the Meuse basin (Belgium). The dolomite is a mixture of calcium carbonate ( $\text{CaCO}_3$ ) and magnesium carbonate ( $\text{MgCO}_3$ ). The chemical composition of the particles is presented in Table 2. For the chemical analysis, the finest particles (below  $40 \mu\text{m}$ ) were eliminated.

The particle size distributions and the characteristic diameters of the particles at the inlet and the outlet of the reactor are detailed in Fig. 4. Despite the finest particles were removed from the bed through the gas extraction due to the elutriation phenomenon (cf. 1.4), the mean particle diameter ( $d_{50}$ ) and the Sauter diameter ( $d_{3,2}$ ) are respectively  $123 \mu\text{m}$  and  $93 \mu\text{m}$  at the inlet, while there are  $90 \mu\text{m}$  and  $70 \mu\text{m}$  at the outlet. This shows the particle size reduction due to the calcination. Since the average density of the particles is around

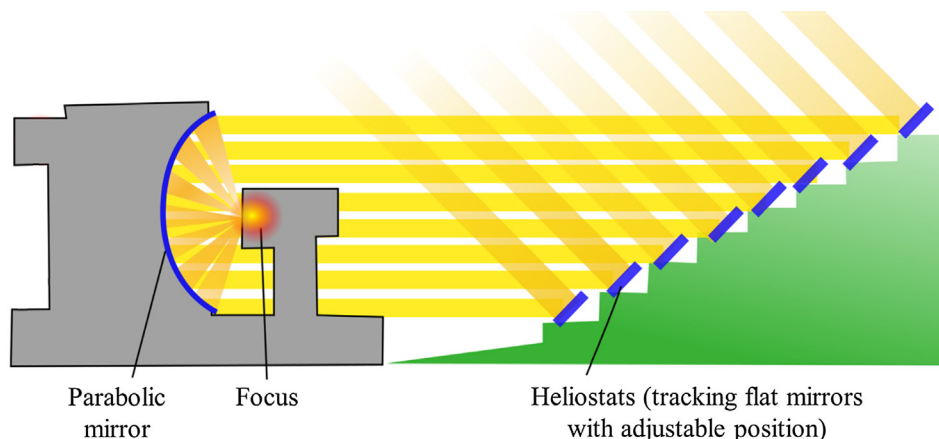


Fig. 2. Working principle of the Odeillo's solar furnace.

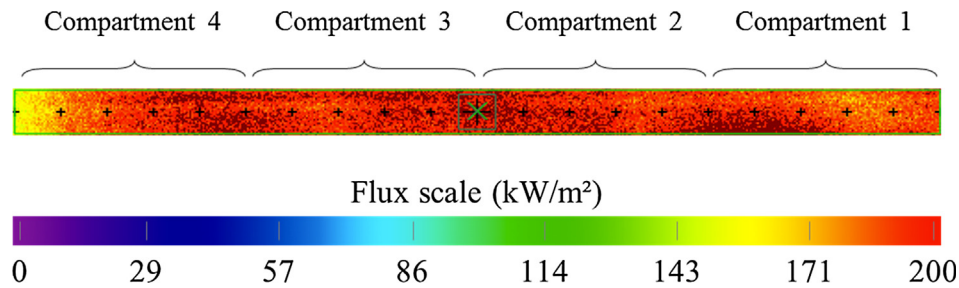


Fig. 3. Flux distribution over the reactor front wall under a DNI of 999 W/m<sup>2</sup>.

**Table 2**  
Chemical composition of the dolomite particles (particles larger than 40 μm).

Chemical composition	Mass fraction (%)
CaCO <sub>3</sub>	55.00
MgCO <sub>3</sub>	44.40
SiO <sub>2</sub>	0.17
Fe <sub>2</sub> O <sub>3</sub>	0.15
Al <sub>2</sub> O <sub>3</sub>	0.05

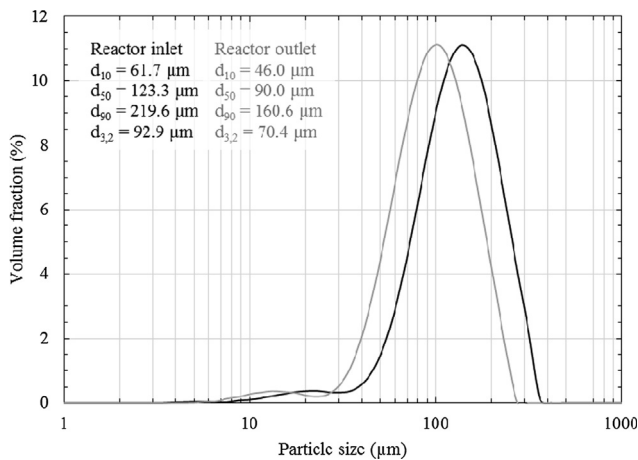


Fig. 4. Particle size distributions at the reactor inlet and outlet.

2850 kg/m<sup>3</sup>, they are classified between Geldart B-type and A-type particles (Geldart, 1973).

#### 4. Numerical model

The numerical model coded with MATLAB aims to compute the wall and particle temperature, and the degree of conversion of the calcination reaction in each compartment of the solar reactor at steady state. For that purpose, each compartment of the reactor is considered as a continuous stirred-tank reactor. The degree of conversion is computed from the reaction kinetics by using mass balances. The temperatures of the front wall of the reactor (receiving the solar flux) and of the fluidized bed are computed by using energy balances. The reaction kinetics depends on the temperature and the endothermic calcination consumes heat, for this reason, it is necessary to use an iterative calculation procedure in order to solve the equations of the model.

##### 4.1. Energy balances

Each compartment of the reactor is modelled according to Fig. 5.

The temperature of the front wall is defined so that the energy balance (1) is fulfilled (the notations are defined in the Nomenclature).

$$\varphi_{\text{abs}} = \varphi_{\text{IR}} + \varphi_{\text{conv}} + \varphi_{\text{FB,F}} \tag{1}$$

The front wall temperature is then used to compute the temperature of the fluidized bed according to energy balance (2).

$$\begin{aligned} & \dot{m}_{p,\text{in}} \cdot \sum_i [y_{i,\text{in}} \cdot H_i(T_{p,\text{in}})] + \varphi_{\text{FB,F}} \cdot S_F \\ &= \Phi_r + \dot{m}_{p,\text{out}} \cdot \sum_i [y_{i,\text{out}} \cdot H_i(T_{\text{FB}})] + \dot{m}_{\text{CO}_2} \cdot H_{\text{CO}_2}(T_{\text{FB}}) + \varphi_{\text{FB,B}} \cdot S_B \\ &+ \dot{m}_{\text{air}} \cdot [H_{\text{air}}(T_{\text{FB}}) - H_{\text{air}}(T_{\text{air,in}})] \end{aligned} \tag{2}$$

To compute the heat fluxes, it is necessary to define the heat transfer

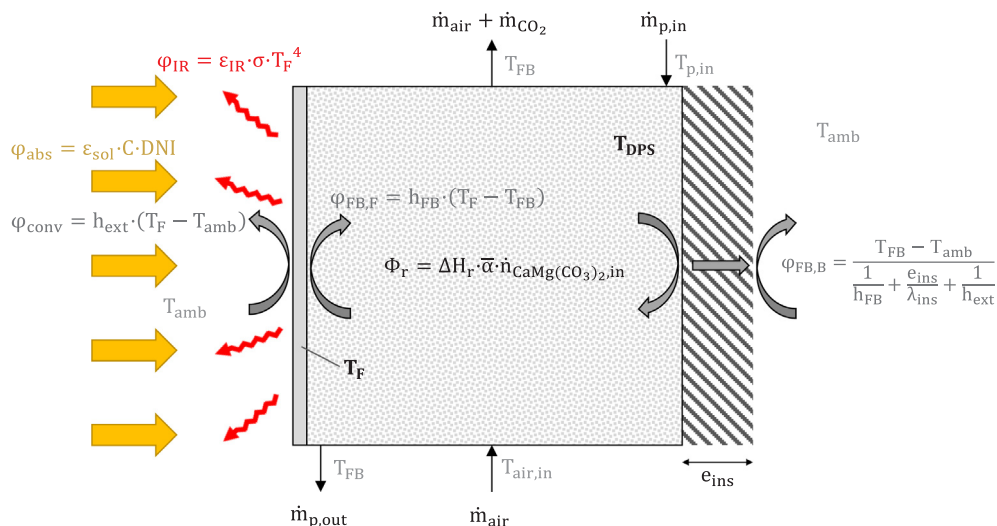


Fig. 5. Diagram of the modelling of a compartment of the solar reactor.

coefficients  $h_{ext}$  and  $h_{FB}$ . The coefficient  $h_{ext}$  accounting for convection between the reactor's walls and the outside atmosphere is taken as  $10 \text{ W}/(\text{m}^2\text{K})$  that is a standard value in such a situation. In any case, this parameter has a second order influence on the energy balance and the model results.

The coefficient  $h_{FB}$  accounting for the heat transfer between the fluidized bed and the reactor walls is a key parameter. However, the bed height (only 10 cm) is not high enough to promote a high fluidization quality with fully developed bubbles at the wall (bubbles movement governs the bed-to-wall heat transfer). Moreover, the high heat flux between the front wall and the fluidized bed affects locally the gas properties and hence the boundary layer and the heat exchange. Therefore, it is not relevant to use empirical correlations from the literature to calculate the heat transfer coefficient  $h_{FB}$ . Consequently, a consistent value of  $h_{FB}$  that enables to fit the model and experimental results is defined.

#### 4.2. Mass balance and mean residence time

The particle mass flow rate at the outlet of a compartment is simply given by the mass balance (3), where the mass flow rate of carbon dioxide produced by the chemical reaction is given by Eq. (4).

$$\dot{m}_{p,out} = \dot{m}_{p,in} - \dot{m}_{CO_2} \quad (3)$$

$$\dot{m}_{CO_2} = \bar{\alpha} \cdot \frac{Y_{CaMg(CO_3)_2,in} \cdot \dot{m}_{p,in}}{M_{CaMg(CO_3)_2}} \quad (4)$$

The mean residence time  $\tau_p$  of the particles in a compartment is computed according to Eq. (5). It accounts for the average mass flow rate of particles (between the inlet and the outlet of the compartment) and assumes a constant volume of particle in the compartment. The volume fraction of particle  $\gamma$  in the compartments is assumed to be 0.40 and does not depend on the chemical composition of the particles. The average density of the particles however, depends on the chemical composition and is given by Eq. (6).

$$\tau_p = \frac{m_p}{\dot{m}_p} = \frac{\gamma \cdot \bar{\rho}_p \cdot V}{(\dot{m}_{p,in} + \dot{m}_{p,out})/2} \quad (5)$$

$$\bar{\rho}_p = \left( \sum_i \frac{Y_i}{\rho_i} \right)^{-1} \quad (6)$$

The quantity of each component in the compartment is computed from the average degree of conversion.

#### 4.3. Reaction kinetics

The reaction kinetics of the partial decomposition of dolomite was estimated by a thermogravimetric analysis (TGA). The aim is to determine the appropriate parameters that enable to compute the reaction rate according to Eq. (7). For that purpose, a sample of dolomite was heated up to  $900 \text{ }^\circ\text{C}$  with a heating rate of  $4.9 \text{ K}/\text{min}$ . The result is depicted in Fig. 6.

$$\frac{d\alpha}{dt} = k(T_{FB}) \cdot f(\alpha) \cdot h(P_{CO_2}) \quad (7)$$

The kinetic law  $f(\alpha)$  which best fits the TGA was determined by the method from Pérez-Maqueda et al., 2002. According to this method, the P4 kinetic law (Eq. (8)) shows the best agreement considering the data corresponding to  $\alpha < 0.7$  (Fig. 7). Above this threshold, the kinetic law is likely to be altered by diffusional effects. Since these effects are negligible in a fluidized bed of fine particles, the corresponding data are not taken into account to determine the kinetic parameters of the reaction.

$$f(\alpha) = 4 \cdot \alpha^{3/4} \quad (8)$$

Then, considering a P4 kinetic law, the pre-exponential factor  $A$  and the energy of activation  $E_a$  of the reaction rate constant  $k(T)$  (expressed according to the Arrhenius law (9)) where fitted to the TGA. The result plotted in Fig. 8 gives  $A = 28.180 \text{ s}^{-1}$  and  $E_a = 85.000 \text{ kJ}/\text{mol}$ .

$$k(T_{FB}) = A \cdot \exp\left(-\frac{E_a}{R \cdot T_{FB}}\right) \quad (9)$$

The additional term  $h(P_{CO_2})$  accounting for the influence of the  $CO_2$  partial pressure is given by Eq. (10). This equation is the most common expression for solid-state decompositions following the stoichiometry (Vyazovkin et al., 2011). As a result, the degree of conversion of the partial decomposition of dolomite is given by Eq. (11). The partial pressure of carbon dioxide in the gaseous phase of the bed is given by Eq. (12).  $P_{eq,CO_2}$  is the partial pressure of carbon dioxide at equilibrium given by the Nernst Eq. (13) in which the Gibbs free energy is computed as a function of the temperature from the enthalpy and the entropy of each substance. For that purpose, the standard enthalpies and entropies, and the polynomial coefficients accounting for the temperature influence are taken from Robie and Hemingway, 1995.

$$h(P_{CO_2}) = 1 - \frac{P_{CO_2}}{P_{eq,CO_2}} \quad (10)$$

$$\alpha = \left[ A \cdot \exp\left(-\frac{E_a}{R \cdot T_{FB}}\right) \cdot \left(1 - \frac{P_{CO_2}}{P_{eq,CO_2}}\right) \cdot t \right]^4 \quad (11)$$

$$P_{CO_2} = \frac{\dot{n}_{CO_2}}{\dot{n}_{CO_2} + \dot{n}_{air}} \cdot P_{amb} \quad (12)$$

$$P_{eq,CO_2} = \exp\left[-\frac{-G_{CaMg(CO_3)_2} + G_{CaCO_3} + G_{MgO} + G_{CO_2}}{R \cdot T_{FB}}\right] \quad (13)$$

In practice, Eq. (11) may lead to degrees of conversion larger than one when  $t$  exceeds the threshold  $t^*$  given by Eq. (14). This is obviously not physical, consequently, above this threshold, the degree of conversion is fixed at  $\alpha_{max} = 1$ .

$$t^* = \frac{1}{k(T_{FB})} \quad (14)$$

Because each compartment of the reactor is modelled as an ideal continuous stirred-tank reactor, the residence time distribution  $E(t)$  of the particles in each compartment is given by Eq. (15) (Rawlings and Ekerdt, 2002) and the average degree of conversion at the outlet of a compartment is computed according to Eq. (16).

$$E(t) = \frac{1}{\tau_p} \cdot \exp\left(-\frac{t}{\tau_p}\right) \quad (15)$$

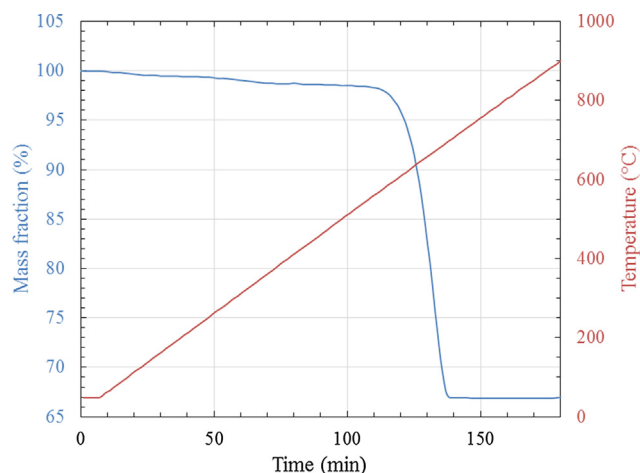


Fig. 6. Thermogravimetric analysis of the partial decomposition of dolomite.

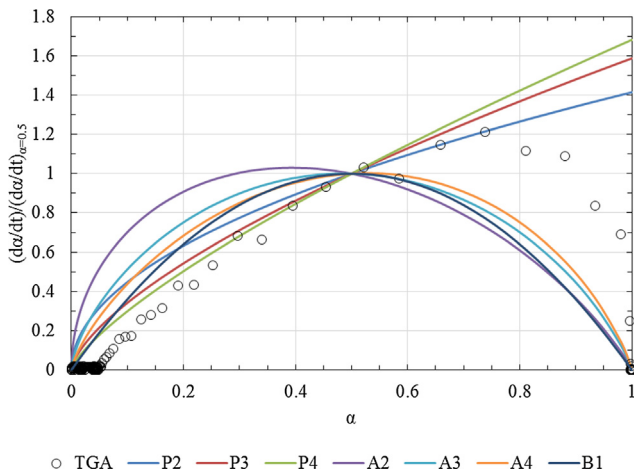


Fig. 7. Determination of the kinetic law corresponding to the TGA by using the method of Pérez-Maqueda et al., 2002.

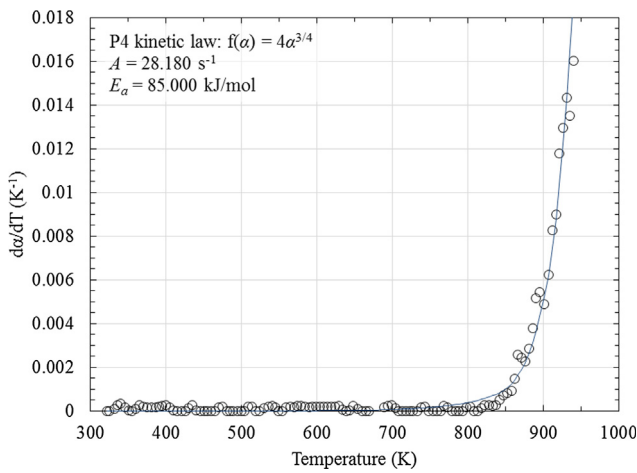


Fig. 8. Determination of the pre-exponential factor and the energy of activation corresponding to the TGA assuming a P4 kinetic law.

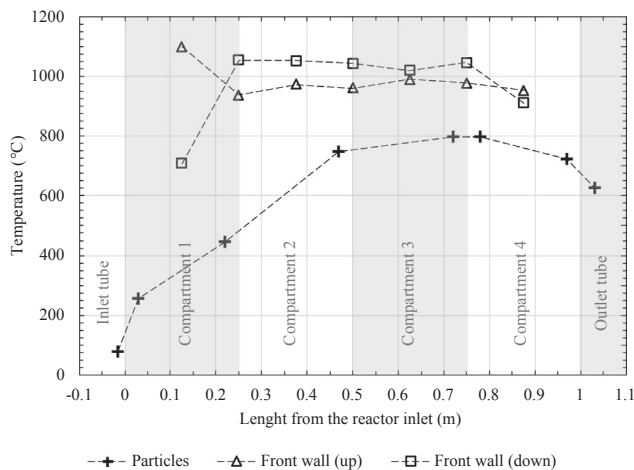


Fig. 9. Longitudinal thermal profiles of the reactor front wall and the particles at steady-state.

$$\bar{\alpha} = \int_{t=0}^{t=\infty} \alpha(t) \cdot E(t) \cdot dt = \int_{t=0}^{t=t^*} \alpha(t) \cdot E(t) \cdot dt + \int_{t=t^*}^{t=\infty} \alpha_{\max} \cdot E(t) \cdot dt \tag{16}$$

Eq. (16) gives the degree of conversion between the inlet and the

outlet of a given compartment  $n$ . The overall degree of conversion  $\bar{\alpha}_{tot,n}$  considered from the reactor inlet and reached at the outlet of the compartment  $n$  is calculated with Eq. (17). In the case considered here,  $\bar{\alpha}_{tot,0} = 0$  because there is no MgO at the reactor inlet.

$$\bar{\alpha}_{tot,n} = \bar{\alpha}_{tot,n-1} + \bar{\alpha}_n \cdot (1 - \bar{\alpha}_{tot,n-1}) \tag{17}$$

#### 4.4. Energy efficiencies

It is possible to define the overall thermochemical efficiency of the reactor as the ratio between the heat consumed by the reaction and the incident concentrated solar power following Eq. (18).

$$\eta_{thch} = \frac{\Phi_r}{C \cdot DNI \cdot S_F} \tag{18}$$

Similarly, it is possible to define the overall thermal efficiency according to Eq. (19). In that case, the energy consumed to heat the particles and the gas is also considered as useful.

$$\eta_{th} = \frac{\Phi_r + \dot{m}_{p,out} \cdot \sum_i [y_{i,out} \cdot H_i(T_{FB})] - \dot{m}_{p,in} \cdot \sum_i [y_{i,in} \cdot H_i(T_{p,in})] + \dot{m}_{CO_2} \cdot H_{CO_2}(T_{FB}) + \dot{m}_{air} \cdot [H_{air}(T_{FB}) - H_{air}(T_{air,in})]}{C \cdot DNI \cdot S_F} \tag{19}$$

### 5. Results and discussion

#### 5.1. Experimental results

Fig. 9 shows the particles temperature measured by thermocouples located at different longitudinal positions of the reactor and centred in height and in width in the fluidized bed. The temperature of particles measured in the inlet and the outlet tubes are also plotted. This thermal profile shows that the first compartment of the reactor is mainly a preheating compartment, while the compartments 2–4 enable to reach a temperature high enough to carry out the half decomposition of dolomite. The temperature measured at the ends of the reactor (0.03 m and 0.97 m from the reactor inlet) show that heat losses and the solar flux distribution (cf. Fig. 3) lead to non-negligible edge effects near the inlet and the outlet. Fig. 9 indicates also the temperature measured by the thermocouples welded on the upper and the lower part of the reactor front wall. Excepted for the first compartment, the temperature of the wall is homogeneously around 1000 °C. The wall of the first compartment exhibits a hot spot caused by fluidization issues. Since the first compartment is at the end of the air distributor, it is poorly supplied with air and hence not well fluidized. As a result, the heat transfer between the reactor wall and the fluidized bed is low and not uniform, which leads to thermal heterogeneities. This also explains why the fluidized bed temperature in the first compartment is significantly lower than in the other compartments.

Fig. 10 shows the transverse thermal profile measured by thermocouples located at 0.47 m from the reactor inlet (i.e. corresponding to the end of compartment 2) and centred in height in the fluidized bed. The temperature measured by thermocouples welded on the upper and the lower parts of the second compartment's front wall. This profile shows that the temperature of the bed is relatively uniform over the transverse cross-section. Because the heat flux is provided to the fluidized bed through the front wall, the temperature of the particles is slightly higher close to the front wall. However, the temperature difference between the two extreme thermocouples is only 42 K.

Considering the total conversion of magnesium carbonates into magnesium oxide at the average temperature of 800 °C (see the reaction enthalpy  $\Delta H_r$ , as a function of temperature in Table 3), the overall thermochemical efficiency of the reactor (Eq. (18)) is 6.6%. This efficiency is in the lower range compared to the thermochemical efficiencies reported from the literature by Moumin et al., 2019 (from 2% to 35%) for the thermal decomposition of calcite, which is a quite

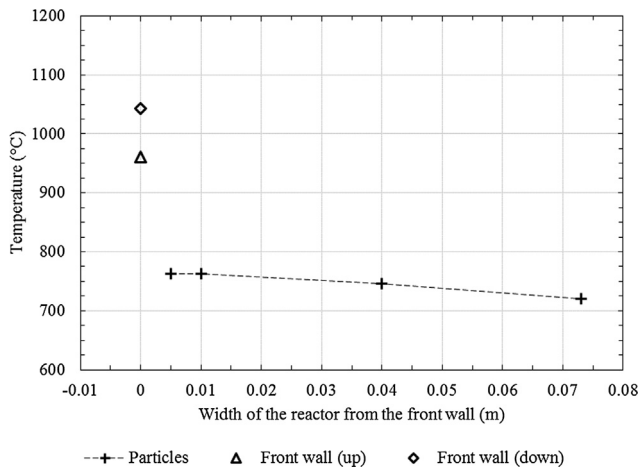


Fig. 10. Transverse thermal profile of the reactor at steady-state.

Table 3  
Input parameters of the numerical model.

A	28.180 s <sup>-1</sup>
[C <sub>1</sub> ; C <sub>2</sub> ; C <sub>3</sub> ; C <sub>4</sub> ]	[195 ; 210 ; 190 ; 195]
DNI	945 W/m <sup>2</sup>
E <sub>a</sub>	8.5000·10 <sup>4</sup> J/mol
e <sub>ins</sub>	0.1 m
h <sub>ext</sub>	10 W/m <sup>2</sup> /K
h <sub>FB</sub>	150 W/m <sup>2</sup> /K
m <sub>air</sub>	4.67·10 <sup>-4</sup> kg/s
m <sub>p,in</sub>	2.62·10 <sup>-3</sup> kg/s
P <sub>amb</sub>	85·10 <sup>3</sup> Pa
T <sub>air,in</sub>	904.8 K
T <sub>amb</sub> , T <sub>p,in</sub>	283.2 K
ΔH <sub>r</sub> (T [K])	(-1.5019·10 <sup>-5</sup> · T <sup>3</sup> + 2.7770·10 <sup>-2</sup> · T <sup>2</sup> - 3.3598·10 <sup>1</sup> · T + 1.3445·10 <sup>5</sup> ) J/mol
ε <sub>IR</sub>	0.95
ε <sub>sol</sub>	0.92
λ <sub>ins</sub>	0.2 W/m/K
ρ <sub>CaCO<sub>3</sub></sub>	2710 kg/m <sup>3</sup>
ρ <sub>CaMg(CO<sub>3</sub>)<sub>2</sub></sub>	2850 kg/m <sup>3</sup>
ρ <sub>MgO</sub>	3580 kg/m <sup>3</sup>

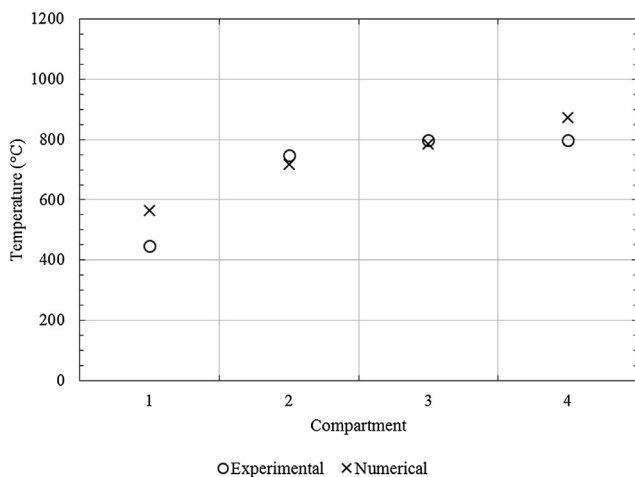


Fig. 11. Comparison between experimental and numerical temperature profiles of the particles.

similar process. This is neither surprising nor critical since the prototype has not been optimised with respect to energy efficiency but designed for the control of particle flow and the front wall solar flux

distribution. The main objective was to run proof of concept experiments to validate the reactor design.

### 5.2. Model results

The experimental data were compared with the results of the numerical model detailed above. For that purpose, the input parameters presented in Table 3 were used.

According to the method presented in 3.1, the heat transfer coefficient between the reactor’s walls and the fluidized bed is set to 150 Wm<sup>-2</sup>K<sup>-1</sup>. Compared to usual fluidized beds, this heat transfer coefficient is low. In fully developed fluidization conditions, values of several hundreds of Wm<sup>-2</sup>K<sup>-1</sup> may be expected (the maximum value obtained with the correlation of Zabrodsky et al., 1976, is 805 Wm<sup>-2</sup>K<sup>-1</sup>, while the average value computed with the correlation of Molerus et al., 1995, is around 210 Wm<sup>-2</sup>K<sup>-1</sup>). This is mainly because the fluidization airflow is not uniform near the gas distributor and the height of the bed is small (only 10 cm). Therefore, the bubbling regime is not fully established and the particle mixing is weak.

The experimental and numerical average temperatures of particles in each compartment of the reactor are compared in Fig. 11. This figure shows that the numerical model gives consistent results compared to the experimental data. However, the model slightly overestimates the particle temperature in the first and the last compartments. This may be due to the edge effects caused by heat losses at the ends of the reactor and the solar flux distribution (cf. Fig. 3) that are not taken into account in the model. Moreover, as it was already mentioned, the fluidization is not good in the first compartment, which reduces the flux absorbed by the fluidized bed and results in an overestimation of the particle temperature in the first compartment.

Fig. 12 shows the comparison between the temperature of the reactor’s front wall computed by the model and the experimental data. The average temperature given by the model is close to the average of the lower and the upper part of the front wall. Once again, the edge effects caused by thermal losses and the flux heterogeneities may explain why the model overestimates the temperature of the fourth compartment’s front wall.

The outlet degree of conversion computed by the numerical model is 96.5% while it is 100% according to the experimental data. This slight difference may be due to the fact that the model computes the degree of conversion at the very outlet of the reactor, while during the experimental tests the particles exiting from the reactor are stored in a tank and cool down before being analysed. During this period, the chemical composition of the particles may vary, e.g. the reaction may go ahead due to the remaining heat. Consequently, a difference of 4.5% between the numerical and the experimental results seems acceptable and may be explained by the uncertainties of both the model and the measured data.

Contrary to experimental data, the numerical model enables to compute the degree of conversion and the efficiency in each compartment. According to the model, the overall thermochemical efficiency (Eq. (18)) is 6.4% and the overall thermal efficiency (Eq. (19)) is 16.8%. For the same reasons as mentioned above (4.1), this thermal efficiency is in the lower range of the values reported by Moumin et al., 2019, for calcite (from 7% to 73%).

The overall degree of conversion, the carbon dioxide mole fraction and the efficiencies computed by the model in each compartment are depicted in Fig. 13. This figure shows that the first compartment exhibits a relatively high thermal efficiency (around 27%) but a degree of conversion (and hence a thermochemical efficiency and a CO<sub>2</sub> concentration) close to zero. This means that the first compartment is mainly dedicated to the sensible heating of the particles, but the temperature is not high enough to carry out the calcination reaction. In the compartments 2 and 3, the particles are injected at high temperature. Therefore, the temperature is high enough to initiate the calcination and an increasing part of the provided heat is consumed by the

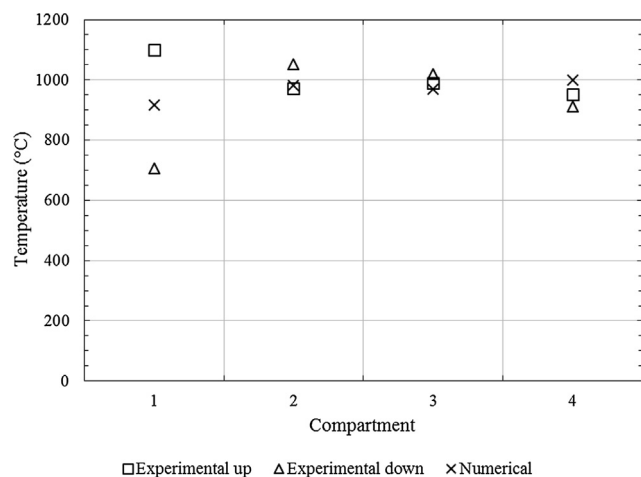


Fig. 12. Comparison between experimental and numerical thermal profiles of the reactor's front wall.

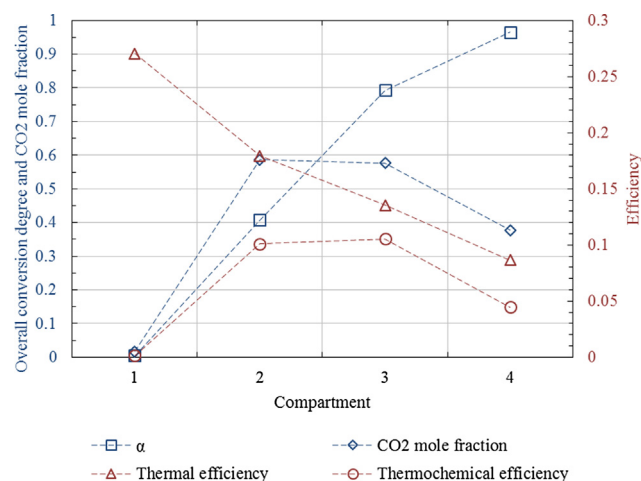


Fig. 13. Model results in each compartment of the reactor.

endothermic reaction. In the compartment 3, the particles are injected almost at the temperature of reaction and most of the useful heat is consumed by the calcination only. As a result, the difference between the thermal and the thermochemical efficiencies (13.5% and 10.5%) is low. According to the model, the CO<sub>2</sub> mole fraction in the compartments 2 and 3 are larger than 55%. At the inlet of the last compartment, more than 79% of the magnesium carbonate has been converted. Therefore, the quantity of reactant converted in the last compartment is lower than in the third one and the equilibrium temperature of the compartment is more governed by the heat losses than by the heat consumed by the reaction. This leads to a decrease of both the thermochemical and the thermal efficiencies in compartment 4.

This validated model is a first step to establish a tool for scaling up this type of fluidized-bed solar reactor. Pilot scale experiments are in progress as the second step of this scaling up approach.

## 6. Conclusion

A compartmented fluidized-bed solar reactor prototype for continuous calcination of mineral particles has been successfully tested at the 1-MW Odeillo's solar furnace (France). During tests carried out with dolomite particles, a particle temperature of 800 °C was reached at steady-state. This led to the half decomposition of 9.4 kg/h of dolomite into magnesium oxide, calcite and carbon dioxide with a degree of conversion of 100%. In these conditions, the resulting thermochemical efficiency was more than 6%. This relatively low efficiency is not

surprising since the pilot reactor has not been fully optimised with respect to energy efficiency. The main objective was to run proof of concept experiments in order to validate the reactor design and the control of the solar flux distribution on the irradiated wall. Further improvements of the thermochemical efficiency is expected using a cavity type receiver-reactor concept.

A numerical model accounting for the energy and mass balances of the reactor and the reaction kinetics successfully simulated the experimental data. This model considered the reactor as a cascade of four ideal continuous stirred-tank reactors. The reaction kinetics of the partial decomposition of dolomite was determined using a TGA.

A larger and improved fluidized-bed reactor of at least 50 kW is currently being tested. It aims at demonstrating the calcination process with calcite, improving the thermochemical efficiency, validating the scaling-up approach and improving the numerical model.

## Declaration of Competing Interest

The authors declare that they have no known competing financial interests or personal relationships that could have appeared to influence the work reported in this paper.

## Acknowledgements

This project has received funding from the European Union's Horizon 2020 research and innovation programme under grant agreement No. 654663, SOLPART project.

This work was supported by the French "Investments for the future", program managed by the National Agency for Research under contract "ANR-10-EQPX-49-SOCRATE" (Equipex SOCRATE).

Authors thank Jean-Louis Sans for the calibration of the solar flux distribution at the focus of the solar furnace and Jan Baeyens for his suggestions.

## References

- Abanades, S., André, L., 2018. Design and demonstration of a high temperature solar-heated rotary tube reactor for continuous particles calcination. *Appl. Energy* 212, 1310–1320. <https://doi.org/10.1016/j.apenergy.2018.01.019>.
- Demir, F., Dönmez, B., Okur, H., Sevim, F., 2003. Calcination kinetic of magnesite from thermogravimetric data. *Chem. Eng. Res. Des.* 81, 618–622. <https://doi.org/10.1205/02638760322150462>.
- Dennis, J.S., Hayhurst, A.N., 1987. The effect of CO<sub>2</sub> on the kinetics and extent of calcination of limestone and dolomite particles in fluidised beds. *Chem. Eng. Sci.* 42, 2361–2372. [https://doi.org/10.1016/0009-2509\(87\)80110-0](https://doi.org/10.1016/0009-2509(87)80110-0).
- Fazeli, A.R., Tareen, J.A.K., 1991. Thermal decomposition of rhombohedral double carbonates of dolomite type. *J. Therm. Anal.* 37, 2605–2611. <https://doi.org/10.1007/BF01912805>.
- Flamant, G., Hernandez, D., Bonet, C., Traverse, J.-P., 1980. Experimental aspects of the thermochemical conversion of solar energy: Decarbonation of CaCO<sub>3</sub>. *Sol. Energy* 24, 385–395. [https://doi.org/10.1016/0038-092X\(80\)90301-1](https://doi.org/10.1016/0038-092X(80)90301-1).
- Geldart, D., 1986. *Gas Fluidization Technology*. John Wiley & Sons.
- Geldart, D., 1973. Types of gas fluidization. *Powder Technol.* 7, 285–292. [https://doi.org/10.1016/0032-5910\(73\)80037-3](https://doi.org/10.1016/0032-5910(73)80037-3).
- Gunasekaran, S., Anbalagan, G., 2007. Thermal decomposition of natural dolomite. *Bull. Mater. Sci.* 30, 339–344. <https://doi.org/10.1007/s12034-007-0056-z>.
- Hashimoto, H., Komaki, E., Hayashi, F., Uematsu, T., 1980. Partial decomposition of dolomite in CO<sub>2</sub>. *J. Solid State Chem.* 33, 181–188. [https://doi.org/10.1016/0022-4596\(80\)90118-8](https://doi.org/10.1016/0022-4596(80)90118-8).
- Haul, A.W., Heystek, H., 1952. Differential thermal analysis of the dolomite decomposition. *Am. Mineral.* 37, 166–179.
- Haul, R.A.W., Markus, J., 1952. On the thermal decomposition of dolomite. IV. Thermogravimetric investigation of the dolomite decomposition. *J. Appl. Chem.* 2, 298–306. <https://doi.org/10.1002/jctb.5010020603>.
- Havryliv, R., Maystruk, V., 2017. Development of combustion model in the industrial cyclone-calciner furnace using CFD-modeling. *Chem. Chem. Technol.* 11, 71–80. <https://doi.org/10.23939/chcht11.01.071>.
- Hehl, M., Helmrich, H., Schugerl, K., 1983. Dolomite decomposition in a high temperature fluidised bed reactor. *J. Chem. Technol. Biotechnol.* 33, 12–24. <https://doi.org/10.1002/jctb.504330103>.
- Imhof, A., 2000. Calcination of limestone in a solar reactor. *ZKG Int.* 53, 504–509.
- Imhof, A., 1997. Decomposition of limestone in a solar reactor. *World Renew. Energy Congr. IV Renew. Energy Energy Effic. Environ.* 10, 239–246. [https://doi.org/10.1016/0960-1481\(96\)00072-9](https://doi.org/10.1016/0960-1481(96)00072-9).
- Kong, W., Wang, B., Baeyens, J., Li, S., Ke, H., Tan, T., Zhang, H., 2018. Solids mixing in a

- shallow cross-flow bubbling fluidized bed. *Chem. Eng. Sci.* 187, 213–222. <https://doi.org/10.1016/j.ces.2018.04.073>.
- Kumar, G.S., Ramakrishnan, A., Hung, Y.-T., 2007. Lime Calcination. In: Wang, L.K., Hung, Y.-T., Shamma, N.K. (Eds.), *Advanced Physicochemical Treatment Technologies*. Humana Press, Totowa, NJ, pp. 611–633.
- Mahasen, N., Smith, S., Humphreys, K., 2003. The cement industry and global climate change: current and potential future cement industry CO<sub>2</sub> emissions. In: Gale, J., Kaya, Y. (Eds.), *Greenhouse Gas Control Technologies - 6th International Conference*. Pergamon, Oxford, pp. 995–1000.
- Mårtensson, R., Bjerle, I., 1996. Thermo gravimetric study of calcination of dolomite at pressurised conditions. *Chem. Eng. Technol.* 19, 364–372. <https://doi.org/10.1002/ceat.270190410>.
- McIntosh, R.M., Sharp, J.H., Wilburn, F.W., 1990. The thermal decomposition of dolomite. *Thermochim. Acta* 165, 281–296. [https://doi.org/10.1016/0040-6031\(90\)80228-Q](https://doi.org/10.1016/0040-6031(90)80228-Q).
- Meier, A., Bonaldi, E., Cella, G.M., Lipinski, W., Wuillemin, D., 2006. Solar chemical reactor technology for industrial production of lime. *Sol. Power Chem. Energy Syst. SolarPACES'04* 80, 1355–1362. <https://doi.org/10.1016/j.solener.2005.05.017>.
- Molerus, O., Burschka, A., Dietz, S., 1995. Particle migration at solid surfaces and heat transfer in bubbling fluidized beds—II. Prediction of heat transfer in bubbling fluidized beds. *Chem. Eng. Sci.* 50, 879–885. [https://doi.org/10.1016/0009-2509\(94\)00446-X](https://doi.org/10.1016/0009-2509(94)00446-X).
- Moumin, G., Tescari, S., Sundarraj, P., de Oliveira, L., Roeb, M., Sattler, C., 2019. Solar treatment of cohesive particles in a directly irradiated rotary kiln. *Sol. Energy* 182, 480–490. <https://doi.org/10.1016/j.solener.2019.01.093>.
- Nikulshina, V., Halmann, M., Steinfeld, A., 2009. Coproduction of syngas and lime by combined CaCO<sub>3</sub>-calcination and CH<sub>4</sub>-reforming using a particle-flow reactor driven by concentrated solar radiation. *Energy Fuels* 23, 6207–6212. <https://doi.org/10.1021/ef9007246>.
- Oates, J.A.H., 1998. *Lime and Limestone: Chemistry and Technology*. Wiley-VCH, Production and Uses.
- Olivier, J.G.J., Janssens-Maenhout, G., Muntean, M., Peters, J.A.H.W., 2016. Trends in global CO<sub>2</sub> emissions: 2016 Report. PBL Netherlands Environmental Assessment Agency.
- Olszak-Humienik, M., Jablonski, M., 2015. Thermal behavior of natural dolomite. *J. Therm. Anal. Calorim.* 119, 2239–2248. <https://doi.org/10.1007/s10973-014-4301-6>.
- Pérez-Maqueda, L.A., Criado, J.M., Gotor, F.J., Málek, J., 2002. Advantages of combined kinetic analysis of experimental data obtained under any heating profile. *J. Phys. Chem. A* 106, 2862–2868. <https://doi.org/10.1021/jp012246b>.
- Rawlings, J.B., Ekerdt, J.G., 2002. *Chemical reactor analysis and design fundamentals*. Nob Hill Publishing, ed., Wisconsin.
- Robie, R.A., Hemingway, B.S., 1995. *Thermodynamic Properties of Minerals and Related Substances at 298.15 K and 1 Bar (10<sup>5</sup> Pascals) Pressure and at Higher Temperatures*. U.S. Geological Survey Bulletin.
- Rodriguez-Navarro, C., Kudlacz, K., Ruiz-Agudo, E., 2012. The mechanism of thermal decomposition of dolomite: New insights from 2D-XRD and TEM analyses. *Am. Min.* 97, 38–51. <https://doi.org/10.2138/am.2011.3813>.
- Samtani, M., Dollimore, D., Alexander, K., 2001. Thermal characterization of dolomite: Kinetic study and effect of procedural variables. *Instrum. Sci. Technol.* 29, 117–132. <https://doi.org/10.1081/CI-100103460>.
- Steen, C.L., Li, K., Rogan, F.H., 1980. Half-calcination of dolomite at high pressures. Kinetics and structural changes. *Environ. Sci. Technol.* 14, 588–593. <https://doi.org/10.1021/es60165a004>.
- Steinfeld, A., Imhof, A., Mischler, D., 1991. Experimental investigation of an atmospheric-open cyclone solar reactor for solid-gas thermochemical reactions. *J. Sol. Energy Eng. Trans. ASME* 114, 171–174. <https://doi.org/10.1115/1.2930001>.
- Stork, M., Meinderstma, W., Overgaag, M., Neelis, M., 2014. *A Competitive and Efficient Lime Industry, Cornerstone for a Sustainable Europe* (Technical report). ECOFYS Netherlands B.V.
- Wulandari, Subagio, W., Adinata, P.M., Fajrin, A., 2017. Thermal decomposition of dolomite under CO<sub>2</sub>-air atmosphere. *AIP Conf. Proc.* 1805. <https://doi.org/10.1063/1.4974427>.
- Thonglimp, V., Hiquily, N., Laguerie, C., 1984. Vitesse minimale de fluidisation et expansion des couches fluidisées par un gaz. *Powder Technol.* 38, 233–253. [https://doi.org/10.1016/0032-5910\(84\)85006-8](https://doi.org/10.1016/0032-5910(84)85006-8).
- Tregambi, C., Salatino, P., Solimene, R., Montagnaro, F., 2018. An experimental characterization of Calcium Looping integrated with concentrated solar power. *Chem. Eng. J.* 331, 794–802. <https://doi.org/10.1016/j.cej.2017.08.068>.
- Valverde, J.M., Perejon, A., Medina, S., Pérez-Maqueda, L.A., 2015. Thermal decomposition of dolomite under CO<sub>2</sub>: insights from TGA and in situ XRD analysis. *Phys. Chem. Chem. Phys.* 30162–30176. <https://doi.org/10.1039/c5cp05596b>.
- Vyazovkin, S., Burnham, A.K., Criado, J.M., Pérez-Maqueda, L.A., Popescu, C., Sbirrazzuoli, N., 2011. ICTAC Kinetics Committee recommendations for performing kinetic computations on thermal analysis data. *Thermochim. Acta* 520, 1–19. <https://doi.org/10.1016/j.tca.2011.03.034>.
- Wen, C.Y., Yu, Y.H., 1966. A Generalized Method for Predicting the Minimum Fluidization Velocity. *AIChE J.* 12, 610–612. <https://doi.org/10.1002/aic.690120343>.
- Zabrodsky, S.S., Antonishin, N.V., Parnas, A.L., 1976. On fluidized bed-to-surface heat transfer. *Can. J. Chem. Eng.* 54, 52–58. <https://doi.org/10.1002/cjce.5450540107>.